HEATING AND ACCELERATION OF CORONAL AND CHROMOSPHERIC IONS DURING SOLAR FLARES

M. E. McKean, R. M. Winglee, and G. A. Dulk

Department of Astrophysical, Planetary and Atmospheric Sciences, University of Colorado, Boulder, CO 80309-0391.

ABSTRACT

One-dimensional, electrostatic, particle-in-cell simulations are used to explore two mechanisms proposed to explain turbulent broadening of soft X-ray emission lines of heavy ions observed during solar flares and the presence of blue-shifted components. Results from the simulations are in qualitative agreement with the observations.

1. INTRODUCTION

Observations of soft X-ray emission lines of heavy ions during solar flares show the presence of energetic turbulent motions in the heavy ions and blue-shifted components (Antonucci et al. 1982; MacNeice et al. 1982; Tanaka 1987). The source of the energy for these phenomena is believed to be the energetic beam electrons produced in the impulsive phase of a flare. The exact mechanism (or mechanisms) that produces the emission line features is a subject of debate. Two such proposed mechanisms, similar in that both utilize superheated electron populations to drive the ion heating, are examined using electrostatic particle-in-cell simulations.

The first mechanism is *in-situ* coronal maser heating (Fig. 1), in which electron cyclotron maser radiation emitted by the energetic electrons is absorbed by ambient coronal electrons (Melrose and Dulk 1982, 1984; McKean, Winglee and Dulk 1989). The heated electrons expand up magnetic field lines in the presence of local density gradients, creating an ambipolar electric field due to the charge separartion between the electrons and the source region ions which then accelerates the ions. It is found that the ambipolar field produces differential ion motion between ion species; this differential motion is unstable to the ion-ion streaming instability, which then preferentially heats and accelerates the

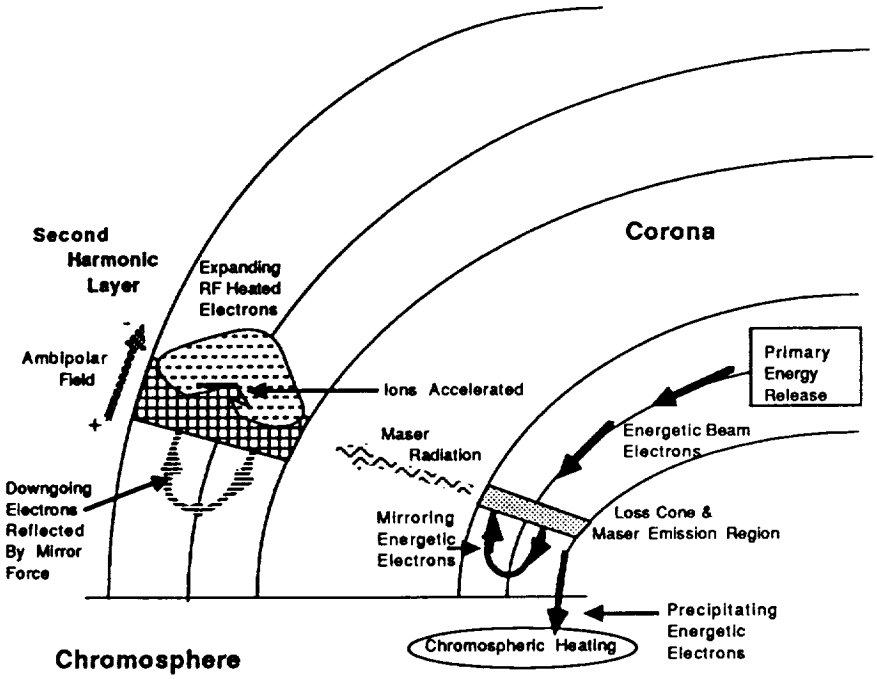

Fig 1: Schematic of coronal maser heating mechanism.

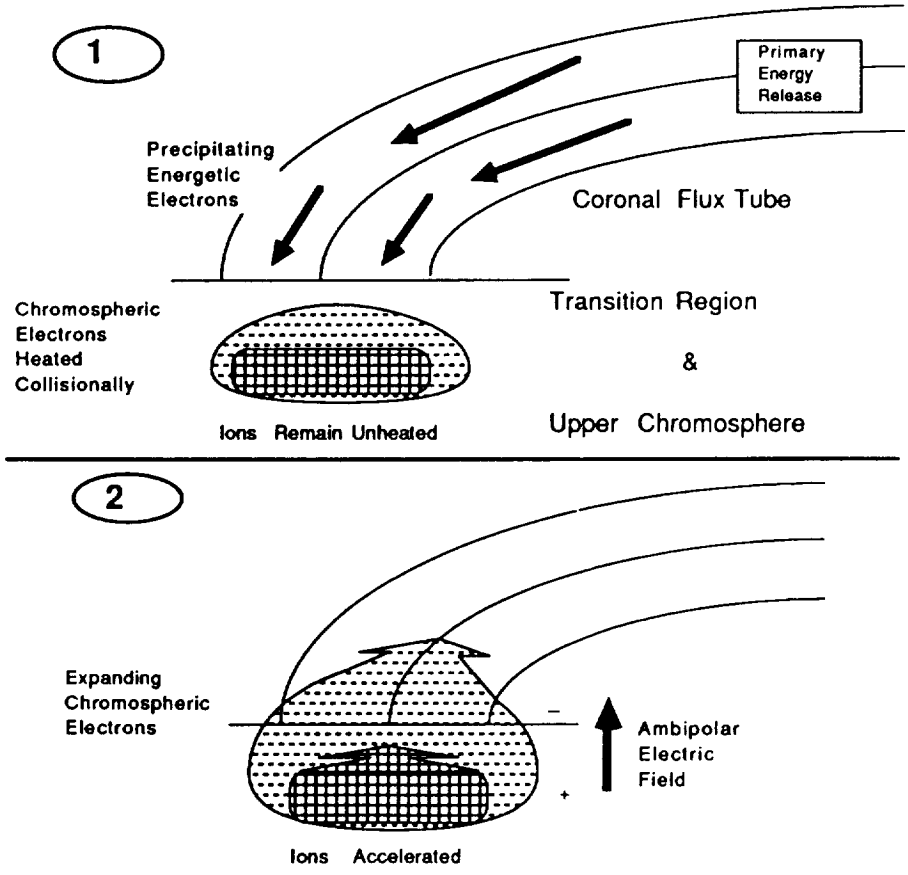

Fig. 2: Schematic of chromospheric heating mechanism.

heavier ion species. The resulting ion distribution functions bear similarities to observed soft X-ray line profiles.

The second mechanism is chromospheric heating (Fig. 2), in which chromospheric electrons are collisionally heated by energetic electrons (Winglee 1989). Under certain conditions, the collisional heating of the chromospheric electrons exceeds the collisional heating of the ions (Winglee 1989); the electrons then expand up field lines into the corona, which results in the formation of an ambipolar electric field and resultant ion acceleration. Heating due to the ion-ion instability is less important in this case, though turbulent-appearing spectra may still be produced due to spatially inhomogeneous ion velocity profiles.

2. SIMULATION MODEL

One-dimensional, electrostatic, particle-in-cell simulations are used in this paper to model the self-consistent evolution of plasma during the outward expansion of a superheated electron population into an ambient plasma at higher altitude and lower density, including the development of an ambipolar electric field and of wave-particle interactions.

The plasma is assumed to have two ion species. One species of ion with mass m_H corresponds to H^+, the dominant species in the solar atmosphere, and accounts for 90% of the total ion number in these simulations. The second ion has a mass $m_{He} = 4\ m_H$, so it is similar in behavior to He^+ or any other ion with $q/m = 1/4$. These heavier ions have a charge-to-mass ratio that roughly corresponds to an ion that has yet to be fully stripped of its electrons. The reason for simulating an ion species that has not yet been fully stripped is that, at the time the ions are being accelerated, they have not been in contact with a population of hot, energetic electrons long enough to have reached an equilibrium, fully stripped ionized state. In order to allow ions to react to electron motion on the time scale of the simulation, it is assumed that $m_H = 100 m_e$, where m_e is the electron mass.

The length of the simulation system (Figure 3) is 2048Δ, where Δ is the simulation cell size. The system is divided into three sections. Between $x = 0$ and $x/\Delta = 384$ lies Region A, which is a region of enhanced plasma density n_A. This region represents the lower corona in the coronal heating simulation and the chromosphere in the chromospheric heating simulation. Between $x/\Delta = 512$ and $x/\Delta = 2048$ lies Region C, which represents the ambient coronal plasma where the plasma density n_C is less than in Region A. Between $x/\Delta = 384$ and $x/\Delta = 512$ lies Region B, where there is a linear change in density between Regions A and C. The enhanced density in Regions A and B, with a hot electron population that has a temperature elevated significantly above the ion temperature, is the ultimate source of the free energy available for the formation of the ambipolar electric field and for the growth of the various instabilities seen in these simulations. Therefore, particles that begin the simulation in Regions A and B are referred to collectively "source region particles." In the chromospheric heating simulation, there is also an ion temperature gradient across Region B, with the ion temperature higher in the corona than in the chromosphere.

The plasma in these simulations is assumed to be collisionless. Particles are reflected after crossing either boundary of the system.

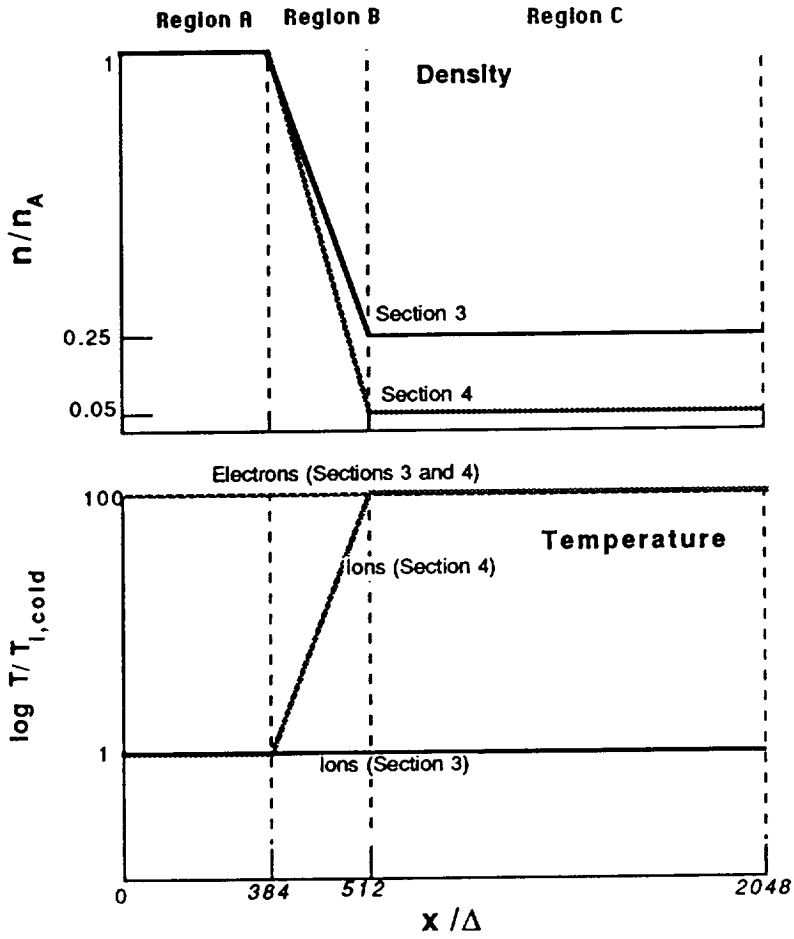

Fig. 3: Schematic model of simulation system showing where Regions A, B, and C lie and the initial ion and electron temperature and density profiles in the two simulations whose results are shown in this paper.

3. *IN-SITU* CORONAL HEATING

The effects of extended *in-situ* coronal heating are examined in this section. The electrons are assumed to be uniformly heated with the temperature uniform through the system and elevated above the ion temperature. Due to the assumed density gradient, there is a pressure excess in the dense region which drives an outward propagating conduction front and subsequent plasma heating. The plasma density changes by a factor of four across Region B, i.e., $n_A/n_C = 4$. The ratio of electron temperature to ion temperature

$T_e/T_i = 100$. The acoustic velocity $c_s = (T_e/m_H)^{1/2} = 1.18\ \omega_H \Delta$, where ω_H is the H^+ plasma frequency in Region A.

The electrons expanding out of the source region set up an ambipolar electric field due to the charge separation between the electrons and the source region ions. The potential drop across the ambipolar field can be inferred from the maxmimum velocity of the reflected electrons, which is about 2 v_{Te}, implying a potential drop of $\sim 4\ T_e$. This potential drop is strong enough to confine the bulk ($\sim 95\%$) of the source region electrons to the region within and behind the ambipolar field.

The ion dynamics is illustrated in Figure 4, which shows the development of the ion phase space, with the H^+ ions in the left column and the He^+ ions in the right column. The initial phase spaces are shown in Figs. 4a and 4b. Once formed, the ambipolar field accelerates both ion species outwards in bulk (Figs. 4c and d). The acceleration of the H^+ ions to high velocities occurs before the He^+ ions because of their higher charge-to-mass ratio; thus the average velocity of the accelerated H^+ is ~ 4 times higher than the same for the accelerated He^+ at $\omega_H t = 30$.

The ambipolar field, initially limited in spatial extent to Region B, expands beyond that region as the footpoints of the field (those points at which the H^+ bulk velocity equals zero) propagate away from Region B at about the local acoustic velocity c_s. By $\omega_H t = 30$, the ambipolar field extends from $x/\Delta \simeq 340$ to $x/\Delta \simeq 560$ (Fig. 4c).

The footpoints represent the movement of the two fronts of the ambipolar field, one of which (a compression front) propagates into and compresses the ambient ions, accelerating them forward; the other (an expansion front) moves into and expands the source region ions, drawing them outward. The two fronts initially overlap; when they separate, a velocity plateau forms in the H^+ phase space (Fig. 4e), and the electric field is zero or near zero in the region of the plateau.

After the fronts separate, the expansion front (marked by the right side dashed line in figures 4c-l) propagates to the left at $\sim 0.65\ c_s$. It constantly expands in size with time because its footpoint moves inward at a higher velocity ($\sim c_s$) than the entire front does. By contrast, the size of the compression front (which is marked by the left side dashed line in Figures 4c-l) front is monotonically reduced (Fig. 4g) until it becomes a narrow, shock-like structure (Fig. 4i, k), with the footpoint of the front moving to the left at $\sim c_s$ and the entire front at $\sim 1.3\ c_s$. The front does not break because, as it steepens, the dispersion of its energy increases and effectively counters the steepening.

By the times in in Figures 4i and k, the front can be described as a shock because there are sharp discontinuities in bulk plasma properties; in other words, large changes in plasma properties such as density and bulk velocity take place across a very narrow region (on the order of an ion acoustic wave wavelength wide). This shock is important because it marks the leading edge of a density wave associated with the expansion of the source region plasma. Its movement through a coronal loop may be seen in spatially resolved X-ray observations because the shock should leave an increased soft X-ray emission in its wake due to the sharply increased numbers of energetic electrons that are confined behind

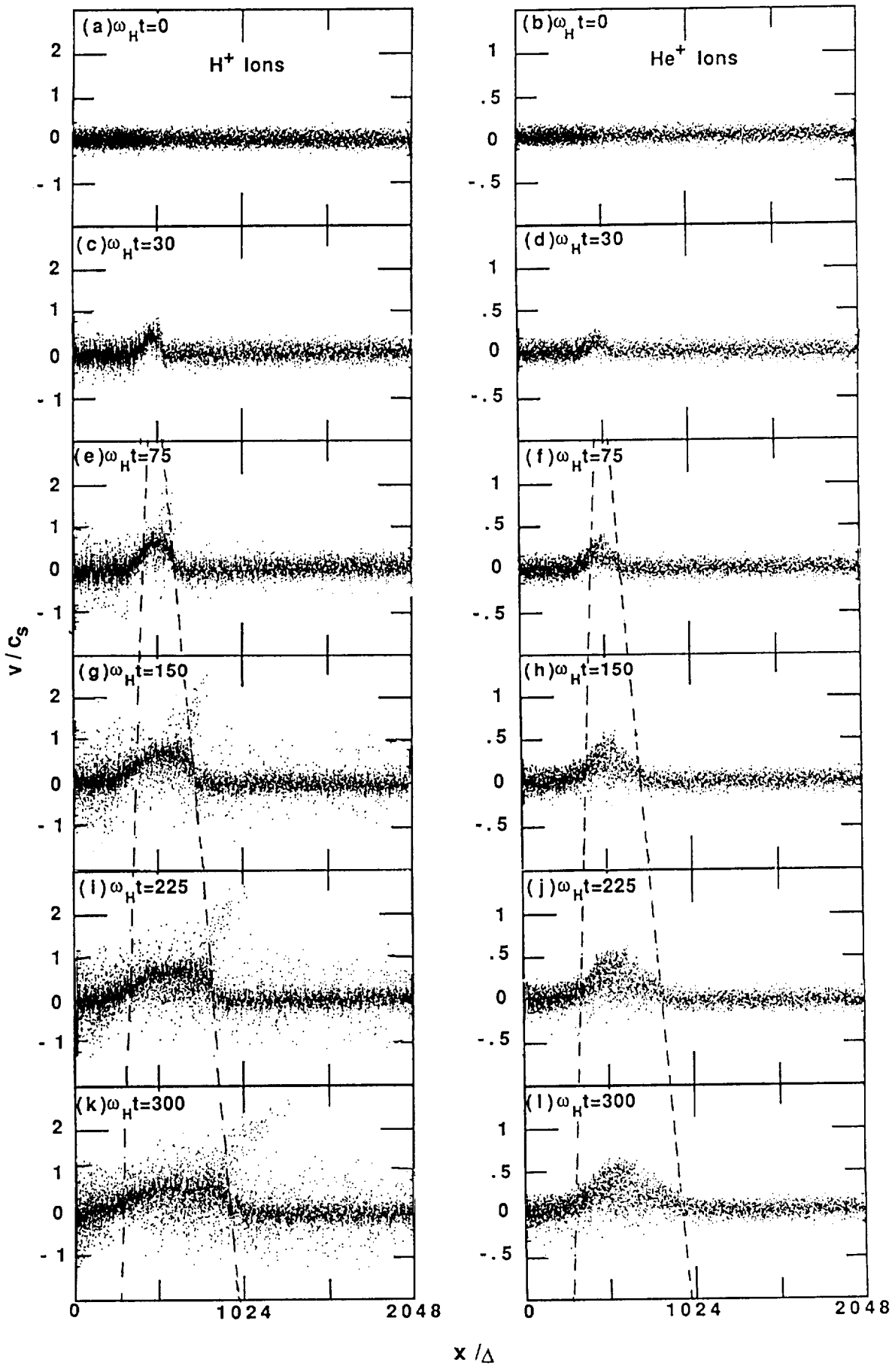

Fig. 4: Ion phase space for coronal heating simulation. Velocities are normalized to the initial acoustic velocity. The propagation of the expansion and conduction fronts are marked by dashed lines.

the shock. Moreover, since it is travelling only at $\sim c_s$, high time resolution is not required to resolve its propagation.

The compression front bears similarities to the ion sound conduction front of Brown, Melrose, and Spicer (1979) in that it confines energetic source region electrons to the region behind the front and reduces the heat flux outwards to a value determined by the velocity of the front, which is of order $\sim c_s$. This limitation of the heat flux is the principle function of a conduction front, which means that the compression front can be identified as a conduction front as well. Because of the different confinement mechanism, it is best described as an "ambipolar field conduction front" to differentiate it from the ion sound conduction front of Brown, Melrose, and Spicer (1979).

The passage of the two fronts through the plasma accelerates H^+ ions to a bulk velocity, hereafter the "beam" velocity, $v_b \simeq 0.65\, c_s$, which corresponds to a "beam" energy of $\sim 0.42\, T_e$. The H^+ ions clearly do not experience the potential drop of $\sim 4T_e$ that the electrons do. The explanation for this apparent discrepancy is that the ambipolar field fronts move through the ions in less time than it would take for an ion to experience the full potential drop if the fronts were stationary. Because of their smaller charge-to-mass ratio and hence mobility, He^+ ions gain less energy than H^+ ions in the potential drop of a front.

Ion acoustic waves excited by expanding heated and return current electrons are manifested as high energy tails in the H^+ ion phase space (Fig. 4e) but not the He^+ phase space (Fig. 4f). These tail ions can reach energies as high as T_e. The highest energy H^+ ions are produced in and close to the conduction front (Figs. 4e and g). This phenomena is a result both of the ambipolar field and of the rapid dissipation of ion waves in this region, which happens because the steep velocity gradient increases the effective temperature of the H^+ ions in the front, thereby reducing T_e/T_i. The dissipated wave energy goes into the production of a population of high energy ions, which are further accelerated through interaction with the ambipolar field. These ions, hereafter called "fast beam ions," can reach velocities as high as $\sim 2.6\, c_s$, or energies of $\sim 7\, T_e = 700\, T_i$ (Figs. 4g, i and k).

The differential motions between the H^+ ions and the He^+ ions can excite an ion-ion streaming instability which transfers energy from the faster to the slower ions. The requirements for this instability to appear in a one-dimensional plasma are (a) that the ratio $T_e/T_i \gg 1$ and (b) that $c_s \geq \Delta u_i > v_t$, where $\Delta u_i = u_H - u_{He}$ is the difference between the H^+ and He^+ bulk velocities and $v_t < c_s$ is the threshhold velocity for the instability (Dusenberry et al. 1988; Winglee 1989). Two important signatures of the ion-ion instability are: (i) nonthermal heating and acceleration of the heavy ions, which produces a distribution function with a broad plateau between the initial H^+ and He^+ bulk velocities and a corresponding increase in the He^+ bulk velocity (Winglee et al. 1989); and (ii) the formation of a large, nonthermal low-energy tail on the H^+ distribution and a corresponding decrease in the H^+ bulk velocity (Winglee et al. 1989; Winglee 1989).

These signatures of the ion-ion instability can be seen at later times in Figure 4. Heavy ions in the beam region and in the fronts have undergone some heating by $\omega_H t = 150$

(Fig. 4h); the velocity dispersion increases further over the remainder of the run (Figs. 4j and l). The heating causes an increase in the maximum velocities of the He^+ ions to the point where they are comparable to the H^+ beam velocity. In the H^+ phase space plots, a low energy tail develops between $v = 0$ and $v = v_b$ in the beam region (Fig. 4g). This low energy tail increases in density with time (Figs. 4i, k).

Figures 5a and b shows the variation of the density with x at $\omega_H t = 0$, 150 and 300 for the H^+ and He^+ ions. The bulk flow of H^+ ions outward reduces the density in the source region, though the simulation ends before any significant depletion occurs at the left boundary. The conduction front is characterized by a sharp jump in H^+ density, which reflects the shock formation at that front. Behind the front, the H^+ ions have a uniform density between $x/\Delta \simeq 450$ and 650 at $\omega_H t = 150$, and $x/\Delta \simeq 450$ and 900 at $\omega_H t = 300$. Thus, in this region, the ambipolar field has destroyed the density gradient, and, since this region corresponds to the velocity plateau in Figures 4g and k, its fronts have left the region.

The He^+ density profile (Fig. 5b) lags the H^+ profile because of the slower bulk movement of these ions. This lag results in an enhancement of He^+ with respect to H^+ in some places (such as at the left end of the H^+ beam region) and a deficiency in others (such as at the conduction front).

The profile of the electron temperature in the region behind the conduction front shows continuous electron cooling throughout the run (Figure 5c). The electrons cool through reflection in the conduction front, the energy loss arising from the rightward movement of the electric field. This energy loss (electron energy is almost all thermal; bulk kinetic energy is a negligible portion of the total) is the source of the free energy driving the ambipolar field and, indirectly, the instabilities. The total energy loss of electrons behind the shock front is $\sim$ 25% at the end of the run, with the minimum temperature being about 50% of the initial electron temperature.

The bulk velocity and effective temperature of the H^+ and He^+ ions is shown in Figure 6 for $\omega_H t = 75$, 150, and 300. The effect of the differential acceleration of the two ion species is evident in Fig. 6a, in which the heavy ions have a peak bulk velocity which is less than half the H^+ peak bulk velocity. The He^+ bulk velocity later increases at the expense of the H^+ bulk motion (Fig. 6b) due to the ion-ion instability. Indeed, by the end of the run (Fig. 6c), the He^+ peak kinetic energy is $\sim$ 1.8 times greater than the H^+ beam region kinetic energy, for the H^+ velocity in the beam region has fallen to $\sim 0.53\ c_s$ and the He^+ peak velocity has risen to $\sim 0.36\ c_s$.

The heating seen in Figures 6d-f is caused by several mechanisms. The H^+ temperature spikes are caused by the presence of fast beam ions, so they are due to an acceleration process which creates a secondary beam of ions rather than to a heating process. The He^+ temperature spikes are signatures of the heating caused by ion-ion turbulence. These spikes are twice as high as the local H^+ temperature in Figures 6e and f, and thus a clear signature of the preferential heating of the heavy ions. Ion acoustic turbulence is responsible for the steady rise in H^+ temperature to the left of the beam region as well as the

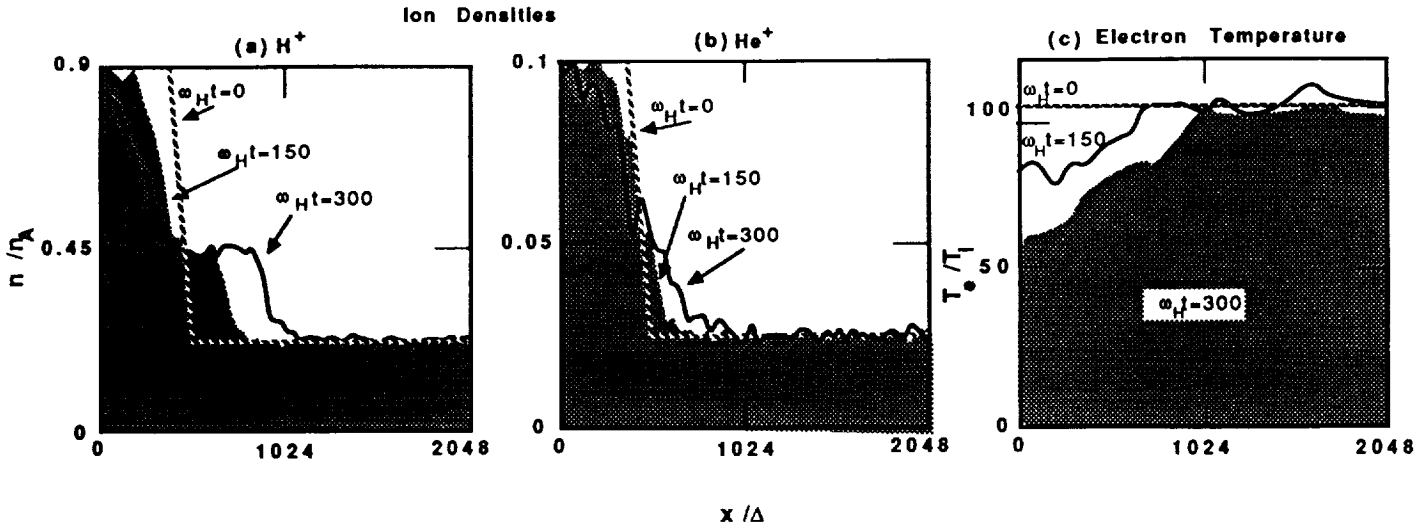

Fig. 5: Ion density profiles for (a) H^+ and (b) He^+ with the density normalized to the initial electron density in Region A. (c) Electron temperature profile with the electron temperature normalized to the initial ion temperature.

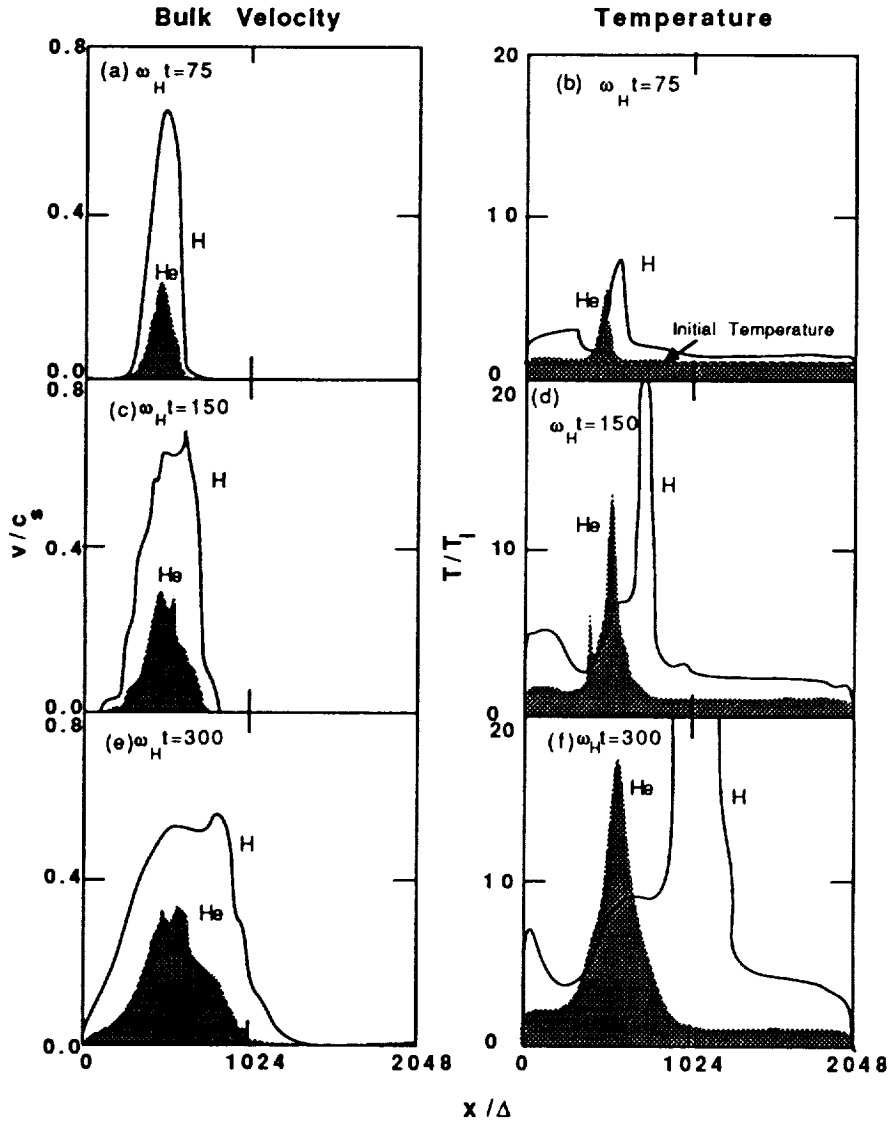

Fig. 6: Ion bulk velocity and temperature profiles. The bulk velocity is normalized to the initial value of the acoustic velocity; the temperature to the initial ion temperature.

rise in temperature in the ambient region to the right of the H^+ spikes. Both ion acoustic and ion-ion turbulence heat the H^+ ions in the beam region and in the fronts.

If the entire simulation system were to correspond to a soft X-ray source region, then distribution functions for the whole system should bear qualitative similarities to soft X-ray line profiles. Figures 7a and b shows such distribution functions for (a) H^+ and (b) He^+ for the beginning, middle and end of the run. Both species have a positive velocity (or blue-shifted) component halfway through the run which grows as a proportion of the total distribution function with time, though it never exceeds the stationary component in size. The H^+ moving component is more substantial; by contrast, the He^+ component is broader and, unlike the H^+ component, increases in velocity with time due to acceleration of H^+ ions by the ion-ion instability. For neither species does the portion of the stationary component for $v < 0$ broaden significantly during the run. For an electron temperature of 10 keV, the effective width of the of the He^+ distribution (about 200 km/s) and the velocity of its blue-shifted component (about 300 km/s), are in rough agreement with velocities inferred from soft X-ray observations. Thus, the ion distribution functions reproduce many, though not all, of the features seen in soft X-ray line profiles.

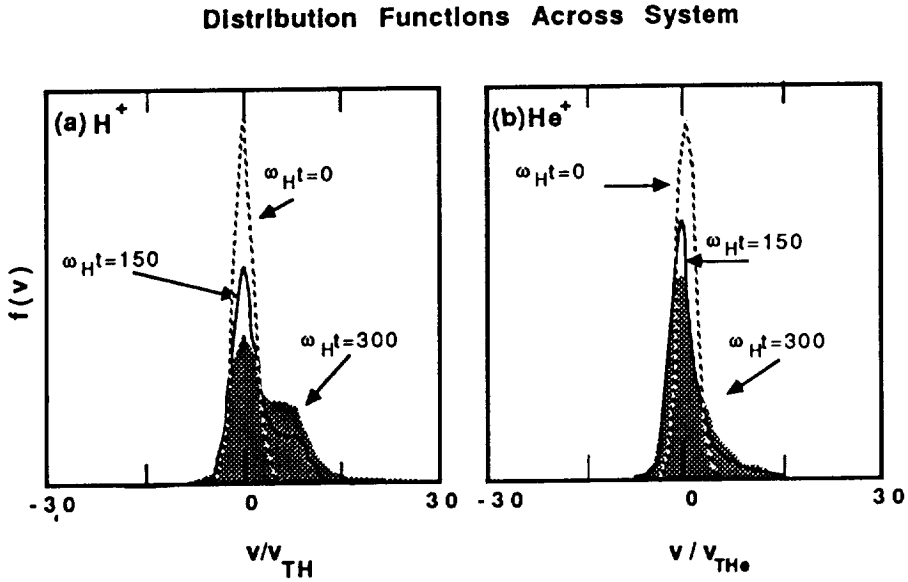

Fig. 7: Ion distribution functions for the entire simulation system. Velocities are normalized to the initial thermal velocities of the two species.

4. CHROMOSPHERIC HEATING

In this section, the acceleration and heating of ions is examined in a case analogous to chromospheric heating. Chromospheric electrons are assumed to be heated to coronal temperatures, so the electrom temperature is uniform through the system, as in Section 3. The electron temperature is elevated with respect to the ion temperature in the chromosphere, but not in the corona, so v_{Ti} is no longer much less than c_s throughout the system, as is true in Section 3. As a result, a pressure excess in the dense region still

drives an outward propagating ambipolar electric field, but no conduction front or density wave forms and little ion heating occurs. The density jump of 20 in this section is larger than in Section 3, a difference that is not examined in detail because simulations run with this density jump but no ion temperature gradient yield essentially the same qualitative features as seen in Section 3. The parameters of the simulation are the same as in Section 3, except $n_A/n_C = 20$, $T_e/T_{iA} = 100$, and $T_e/T_{iC} = 1$.

The ion phase space diagrams are shown in Figure 8. Figures 8a and b are the initial phase space plots of the H^+ and He^+ ions respectively. As in the coronal case, the source region ions are accelerated outwards by the ambipolar field created by the expansion of the heated source region electrons. A difference from the previous simulation is that the ambient, or coronal, ions are not swept outward by a conduction front. Instead, many of the coronal ions are able to penetrate the ambipolar field region (delimited by the dashed lines in Figures 8c-f) because, since the coronal ion thermal velocity $v_{TiC} \sim c_s$, they have sufficient kinetic energy to overcome the potential energy barrier the field region represents. As a result, no conduction front or shock front forms, and neither does a density wave (Figs. 8c, e, and g).

The region containing the ambipolar field initially confined to the transition region, penetrates deeply into both the chromosphere and corona during the run. The left edge of the field region propagates to $x/\Delta \simeq 128$ by the end of the run, with an average velocity of $\sim 0.7\ c_s$. The right edge (indicated by the right side arrows) propagates to $x/\Delta \simeq 1280$ by $\omega_H t = 300$ for an average velocity of $\sim 2.5\ (T_e/m_H)^{1/2}$, which is only slightly greater than the local sound speed once the ion temperature is taken into account. While the field region expands, the potential drop across it remains roughly constant ($\sim 4\ T_e$), so the average field strength in the region decreases monotonically with time.

The initial velocity of many transition region ions matches or exceeds that of the outgoing electric field, whose velocity averages $\sim 1.2 c_s$. As a result, these ions are accelerated more efficiently by the ambipolar field, i. e., they gain more energy in the potential drop of the field than slower ions, in a fashion similar to the mechanism that produced the fast beam ions of the last section. For example, transition region H^+ ions that begin with a velocity of $\sim c_s$ in Figure 8a, have been accelerated to a velocity of $> 2\ c_s$ in Figure 8e, an energy gain of $> 3T_e$. Initially fast He^+ ions are likewise accelerated efficiently; ions that begin with a velocity of $\sim 0.5\ c_s$ (Fig. 8b) are accelerated to velocities of $\sim 0.8\ c_s$, an energy gain of $\sim 2\ T_e$. These fast ions form the leading edges of the outfowing ion "beams."

The effects of the ion-ion streaming instability are visible in the phase space plots of both ion species. The velocity dispersion of source region He^+ ions to the right of $\sim x_1$ is increased between $\omega_H t = 75$ and 150 (Figs. 8d and f) due to the instability, and increases further between $\omega_H t = 150$ and 300 as ion-ion turbulence grows in strength. This heating is accompanied by a weak low energy tail in the H^+ beam (Fig. 8g). The heating of both species is weaker than in the coronal case due to the presence of hot coronal ions which effectively decrease the ratio of T_e/T_i and thereby suppress the ion-ion instability.

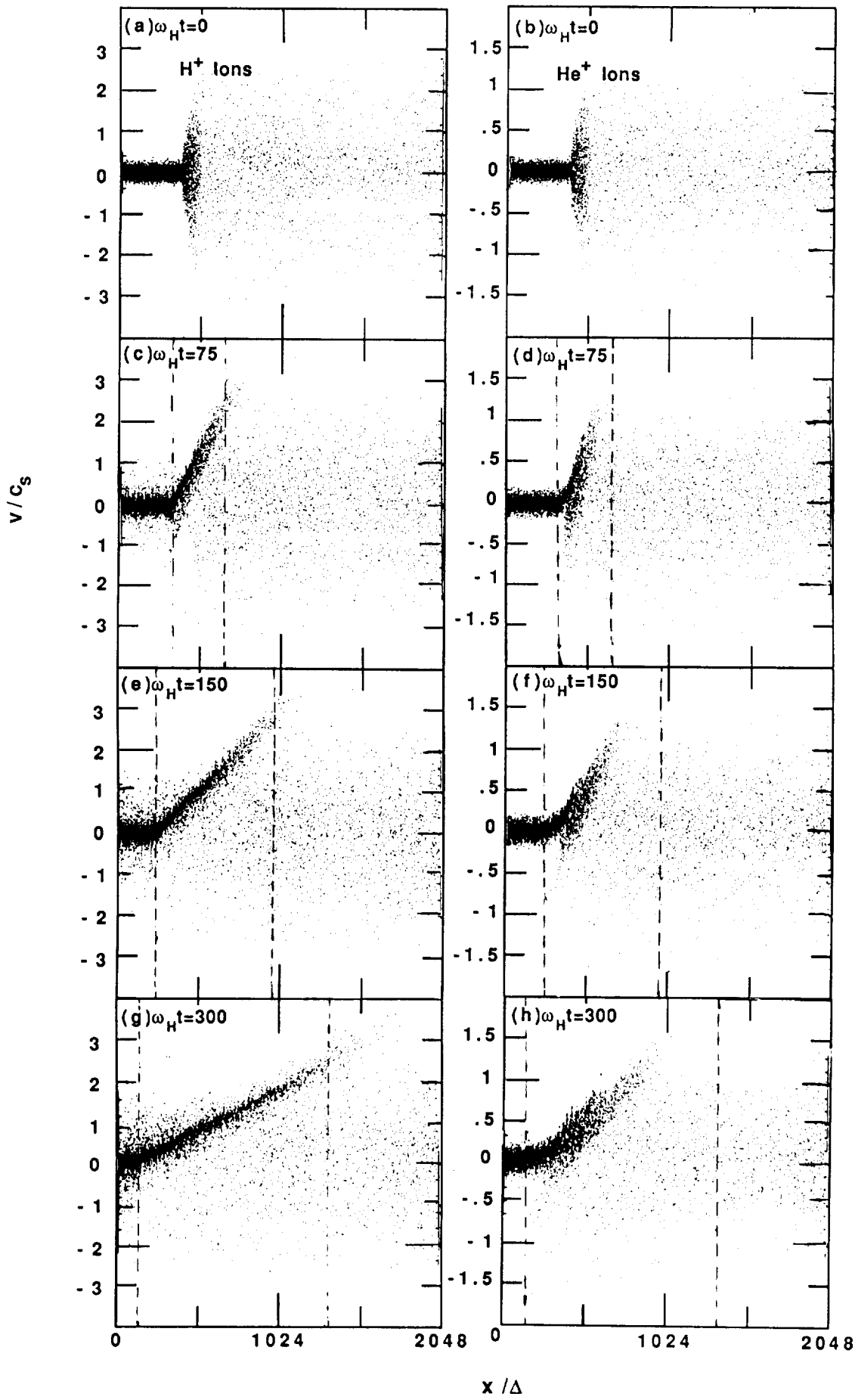

Fig. 8: Ion phase space for chromospheric heating simulation. Velocities are normalized to the initial chromospheric acoustic velocity. The region containing the ambipolar electric field is delimited by dashed lines.

Figure 9 shows the bulk velocity and temperature profiles of the chromospheric and transition region ions only, since these parameters for the coronal ions remain largely unchanged over the course of the run. The ambipolar field more readily accelerates the faster transition region ions to high velocitie than the slower transition region and chromospheric ions. Such an acceleration hierarchy results in outflowing particle beams with monotonically increasing bulk velocity profiles for both ion species (Fig. 9a). The H^+ beam is more extended than the He^+ beam because of the greater velocity of the H^+ ions. The peak kinetic energy of the He^+ ions initially is also smaller than the H^+ peak energy due to the more gradual acceleration of He^+ ions by the ambipolar field (Fig. 9a). As the leading edge of the He^+ ion beam undergoes further acceleration, its velocity becomes half that of, and represents the same kinetic energy as the peak H^+ velocity (Fig. 9c).

The heating caused by the ion-ion instability is evident in Figures 9c and d, in which the He^+ temperature exceeds the H^+ temperature between $x/\Delta \simeq 400$ and 700 in Figure 9c, and between $x/\Delta \simeq 300$ and 900 in Figure 9d (the H^+ heating actually is due more to ion acoustic turbulence than ion-ion turbulence). The extent of the heavy ion heating grows between $\omega_H t = 150$ and 300, indicating that ion-ion turbulence peaks in strength after $\omega_H t = 150$.

In order to compare these results to soft X-ray line emissions, we examine the distribution functions of the two ion species, which are shown in Figure 10 (H^+ in Fig. 10a, He^+ in Fig. 10b). As seen previously in the coronal case (Fig. 7), the blue-shifted component of both ion species increases in size as the run continues, with that of H^+ consisting of a greater proportion of the total distribution function than the blue-shifted component of He^+ at any time $t > 0$. The central difference is that the velocity of the peak of the blue-shifted component increase with time in both distributions rather than just the He^+ distribution due to the continuous acceleration over time of source region ions by the ambipolar field. The effective temperature, or velocity dispersion, of the blue shifted components of both species also appears to increase with time, to a value approaching T_e by the end of the run. The broadened distributions bear close qualitative similarities to the distribution functions for the coronal heating simulation (Fig. 7). However, if one assumes that the electron temperature is 100 eV, the effective thermal velocity of the He^+ distribution, as well as the velocity of the moving component, is only about 50 km/s, which is too low to explain the observations, however.

5. CONCLUSION

Ion heating associated with the expansion of hot electron populations in both coronal chromospheric applications during solar flares have been analyzed using particle simulations as methods of reproducing heavy ion soft X-ray line features observed during solar flares; specifically, nonthermal line broadening and the presence of blue-shifted components. In the simulations, the expansion of heated electrons across density gradients is

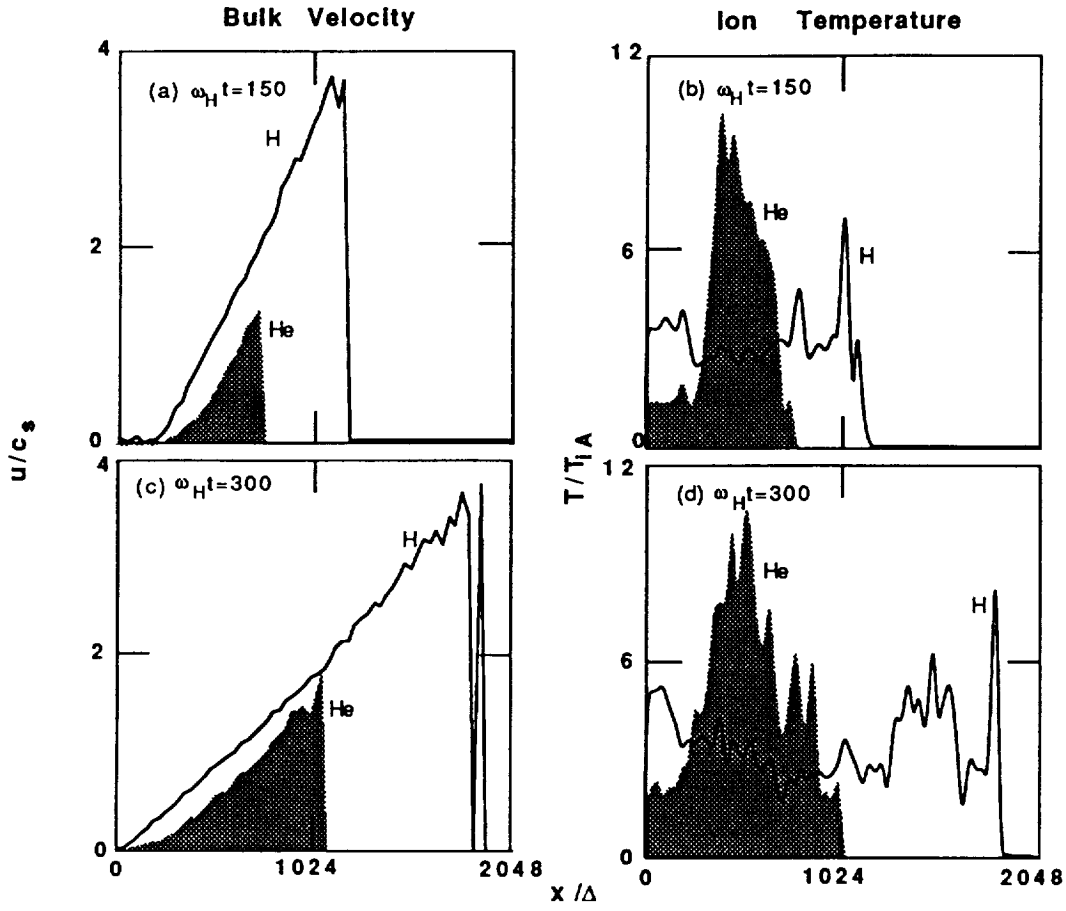

Fig. 9: Ion bulk velocity and temperature. The bulk velocity is normalized to the initial chromospheric acoustic velocity; temperature, to the initial chromospheric ion temperature.

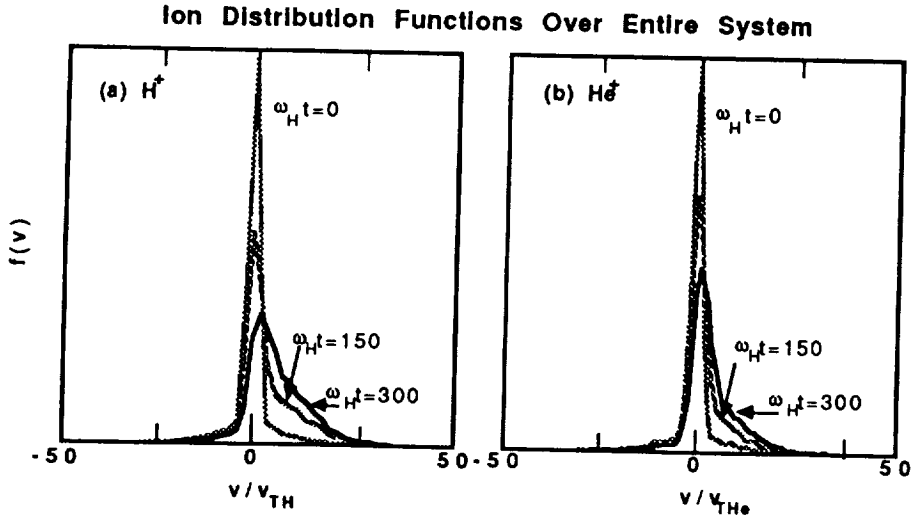

Fig. 10: Distribution functions for all the ions in the simulation system. Velocities are normalized to initial chromospheric thermal velocities.

found to create an ambipolar electric field which is capable of accelerating ions up to energies of order the lectron thermal energy. In the coronal case, the H^+ ions form a constant velocity and density beam region between forward and backward propagating fronts of the ambipolar field, the forward front eventually steepening into an electrostatic shock. The ions in the beam region are unstable to the ion-ion streaming instability, which then acts to preferentially heat and accelerate the He^+ jions by extracting the H^+ beam energy. This nonthermal heating as well as the acceleration is clear in the ion distribution functions, which bear some similarity to soft X-ray line profiles. In the chromospheric case, no similar beam region is formed, the ion-ion instability is weaker, and little preferential heavy ion heating occurs. However, substantial broadening is present in the ion distribution functions due to the nonuniform motion of the ions. Thus, these simulations have been able to reproduce some of the features, though not all, of soft X-ray line emissions. Only in the coronal heating simulation are the broadening and the speed of the blue-shifted component in agreement with soft X-ray line observations.

Future work on this project includes the addition of a heavy ion with a charge to mass ratio of about 2 to represent those ions actually emitting the soft X-rays, and the addition of a method to simulate the continuous heating of the system by energetic electrons.

This work was supported by National Science Foundation grant ATM-8719371 and by NASA's Solar Terrestrial Theory and Solar Heliospheric Physics Programs under grants NAGW-91 and NSG-7287 to the University of Colorado. The simulations were performed on the CRAY X-MP at the San Diego Supercomputer Center which is supported by the National Science Foundation.

REFERENCES

Antonucci, E. (and 8 others) 1982, *Solar Phys.*, **78**, 107.
Brown, J. C., Melrose, D. B., and Spicer, D. S. 1979, *Ap. J.*, **228**, 592.
Dusenberry, P. B., Martin, R. F., and Winglee, R. M. 1988, *J. Geophys. Res.*, **93**, 5655.
MacNeice, F. (and 8 others) 1985, *Solar Phys.*, **99**, 167.
McKean, M. E., Winglee, R. M., and Dulk, G. A. 1989, *Solar Phys.*, in press.
Melrose, D. B., and Dulk, G. A. 1982, *Ap. J. (Letters)*, **259**, L41.
Melrose, D. B., and Dulk, G. A. 1984, *Ap. J.*, **282**, 308.
Winglee, R. M. 1989, *Solar Phys.*, in press.